

High Power Semiconductor Red Laser Arrays for Use in Photodynamic Therapy

Ivan Charamisinau, Gemunu Happawana, Gary Evans, *Member, IEEE*, Jay Kirk, David P. Bour, Arye Rosen, and Alex R Hsi

Abstract— Semiconductor laser ridge arrays emitting 250 mW at a wavelength of 635 nm are designed for photodynamic therapy applications. Although ridge laser arrays are less efficient than broad area lasers, they are more reliable and can produce higher power from the same lateral width due to thermal considerations. An analytic expression for the active layer temperature of the laser array as a function of the ridge spacing, number of ridges and width is derived and has excellent agreement with a finite element analysis. This analytic expression allows optimization of the laser and the submount geometry to minimize the active region temperature with the constraint of a small submount, heatsink and package.

Index Terms— Photodynamic therapy, Diode laser array, Thermal modeling, High power red lasers

I. PHOTODYNAMIC THERAPY

Many types of cancer can be treated by photodynamic therapy (PDT), which destroys cancer cells through the use of light in combination with a photosensitizing drug. The drug is administered to the patient many hours before treatment and accumulates mainly in cancerous cells [1]. Illuminating the cancerous area activates the drug and kills the cancerous cells, with little damage to surrounding healthy tissue in which there is only a modest concentration of the drug. As a result, the cumulative toxicity associated with repeated ionizing radiation treatments [2,3] can be largely avoided with PDT.

Presently porfimer sodium is the most common photosensitizer used for PDT since it has been extensively studied and approved by U.S. Food and Drug Administration (FDA). Photofrin is activated by 630 to 635 nm light and has successfully treated almost all cancers, including breast, bladder, colon, esophageal, gynecologic, head, lung, neck, prostate, and skin cancer. The choice of ~ 635 nm light is a

Manuscript received May 25, 2004. This work was supported in part by the U.S. AMT, Inc. under Grant BS123456. I. Charamisinau is with Southern Methodist University, Dallas, TX 75275 USA (corresponding author to provide phone: 214-768-1966; fax: 214-768-1473; e-mail: icharami@engr.smu.edu).

G. Happawana is with Southern Methodist University, Dallas, TX 75275 USA (e-mail: happawan@engr.smu.edu)

G. Evans is with Southern Methodist University, Dallas, TX 75275 USA (e-mail: gae@engr.smu.edu)

J. Kirk is with Southern Methodist University, Dallas, TX 75275 USA (e-mail: kirk@engr.smu.edu)

D. P. Bour is with Agilent Technologies (e-mail: dave_bour@exeh.labs.agilent.com)

tradeoff between light penetration through tissue and blood and absorption by photofrin[12].

Lasers used for PDT include gold vapor, tunable dye lasers, copper vapor, frequency doubled Nd:YAG and excimer lasers. Semiconductor diode lasers, which are much smaller and cheaper than other lasers, are ideal for PDT.

II. LIGHT DELIVERY SYSTEMS

There are two approaches to delivering light from semiconductor lasers to tumors. One method is direct illumination by semiconductor laser arrays contained in a balloon catheter. The second method couples the semiconductor laser light to an optical fiber that contains a Bragg grating or diffusing region over a portion of the fiber to couple the light out and direct it towards the tumor. Both approaches have their advantages and challenges. Fibers allow light delivery to tumors located in the interior of the lung or brain with relative ease, since the fiber has a small diameter (100 to 500 μm). However, coupling high power light from many lasers into a single fiber requires precision alignment techniques that may degrade with time. The balloon catheter approach is particularly useful for esophagus cancer [4-6].

Placing the diode lasers in a balloon catheter and directly illuminating the tumor avoids fiber coupling losses and critical alignments. Numerous lasers can illuminate the tumor so high powers can be achieved and tumors of any size can be illuminated. Electrical control to individual lasers or subgroups of lasers allows custom illumination patterns to achieve maximum treatment efficiency.

III. RIDGE WAVE-GUIDE (RWG) LASERS ARRAYS

Fabrication of high power lasers [13] at the 635 nm wavelength that activates porfimer sodium is challenging because of the reduced electron confinement in the quantum well compared to longer wavelengths such as 650 or 680 nm[9]. The few commercial products are high power 635 nm broad area lasers in the 100-500 mW range and require operation at or below 15C. The power required from each laser depends on the number of lasers used for the PDT treatment and the treatment time. Typical PDT applications require a total power of ~ 4 watts with individual lasers (or laser subarrays) emitting ~ 200 mW.

AlGaInP/GaAs 635 nm laser design is a compromise between low threshold currents and large beam divergences.

However, for PDT applications, a large beam divergence is desirable. WAVEGUIDE [8] software, which uses a transfer matrix method to find the near- and far- fields of laser structures, was used to determine the optimum epitaxial structure to achieve the maximum quantum well confinement factor. The actual and ideal laser structures are given in Table 1 and the corresponding index profile and field distribution are shown in Fig. 1. The theoretical perpendicular beam divergences is about 40 degrees for both cases and is in reasonable agreement with the experimental measurement of 42 degrees. The performance of the actual structural is very close to the theoretical optimum structure as shown in Table 2 with only a slight difference in beam divergence and threshold current.

The threshold current in Table 2 is calculated for a 500 μm cavity length which is close to the optimum cavity length (L_{opt}) of 428.6 μm calculated from [13]:

$$L_{opt} = \frac{1}{2G_0} \ln \frac{1}{R_1 R_2} \quad (1)$$

where R_1 and R_2 are facet reflectivities, both equal to 0.3 and the modal gain parameter G_0 is 27.98 cm^{-1} , calculated by GAIN [14] for the structures in Table 1.

TABLE I
MATERIAL COMPOSITION OF EPI STRUCTURE[9]

#	Layer name	635 nm Epitaxial Structure	
		Material	Actual/Ideal Thickness, μm
1	P+cap	GaAs	0.05
2	Barrier reducer	$\text{Ga}_{0.5}\text{In}_{0.5}\text{P}$	0.075
3	p-cladding	$\text{Al}_{0.5}\text{In}_{0.5}\text{P}$	0.75
4	Etch stop	$\text{Ga}_{0.6}\text{In}_{0.4}\text{P}$	0.004
5	p-spacer	$\text{Al}_{0.5}\text{In}_{0.5}\text{P}$	0.25
6	SCH	$(\text{Al}_{0.6}\text{Ga}_{0.4})_{0.5}\text{In}_{0.5}\text{P}$	0.1063/0.09
7	QW	$\text{Ga}_{0.5}\text{In}_{0.5}\text{P}$	0.0080
8	SCH	$(\text{Al}_{0.6}\text{Ga}_{0.4})_{0.5}\text{In}_{0.5}\text{P}$	0.1063/0.09
9	n-cladding	$\text{Al}_{0.5}\text{In}_{0.5}\text{P}$	1
10	Substrate	GaAs	~ 100

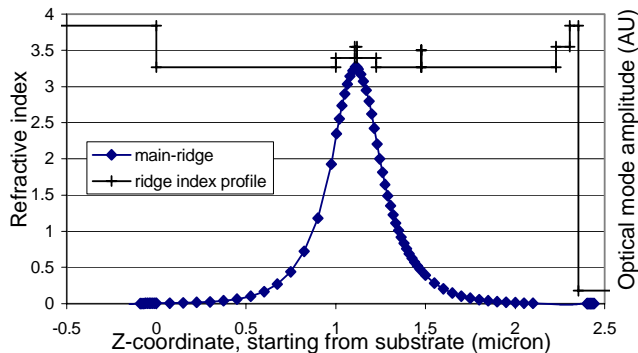


Fig. 1. Index profile and near-field of the as grown structure (Table 1).

TABLE II.
COMPARISON OF A REAL LASER STRUCTURE
TO IDEAL OPTIMIZED

	As (theory)	Grown (theory)	Ideal (theory)	Mea- sured
quantum well confinement factor Γ	3.0289%	3.0558%	-	-
perpendicular far-field divergence	40.0°	41.5°	42°	-
near-field width	0.2284	0.2181	-	-
threshold current J_{th}	21.7 mA	21.3 mA	-	27-41mA

Further improvements to the laser performance at high power can be obtained by minimizing the temperature rise at the quantum well active region. Although broad area lasers (typically 100 μm wide by 500 μm long) make efficient use of the injected current, the heat is highly localized. Broad area lasers are also subject to unstable optical filaments, which in association with the high temperatures results in catastrophic optical damage (COD). Ridge wave-guide lasers (RWG), which are slightly less efficient than broad area lasers, confine the optical power to a stable, narrow region. By spreading out many narrow (~ 5 μm wide by 500 μm long) RWG lasers in an array (see Fig. 2), the temperature rise of the quantum well can be reduced while maintaining high power output.

In this array design, the average heat generation per unit area is significantly lower than in a broad area laser and the maximum active region temperature is reduced, allowing high power operation and longer life.

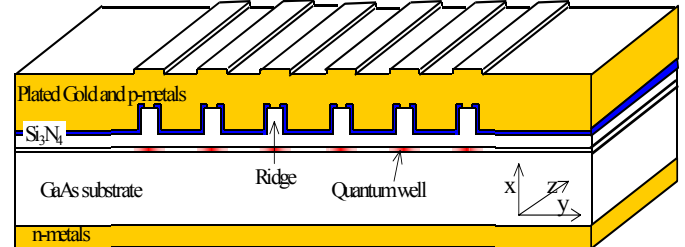


Fig. 2. Laser array.

The number of ridges, ridge widths and ridge spacings are considered in optimizing the array. The optimum values of these design parameters depend on multiple factors which include the laser efficiency, lateral (y) near field, thermal resistance between the active region and the heat sink, fabrication processes and packaging.

To insure a single lateral mode, the width of the ridge should be less than $d_{2,c}$, (the cut-off ridge width for the second mode) where

$$d_{2,c} = \frac{\lambda}{2\sqrt{n_{ridge}^2 - n_{wing}^2}} = 3.78 \mu\text{m}, \quad (2)$$

where λ is the wavelength (635nm), n_{ridge} is the effective index under the ridge region, n_{wing} is the effective index between the ridges. For the structure in Table 1, WAVEGUIDE [8] calculations give $n_{ridge} = 3.329233$ and $n_{wing} = 3.328174$.

Because the high order lateral modes extend further beyond the ridge than the lowest order mode, their overlap with the gain region is much lower as long as the ridge width is less than about $6\ \mu\text{m}$, as shown in Fig. 3, which suggests that even ridge widths in the 4 to $6\ \mu\text{m}$ range will result in single lateral mode operation. Such ridge lasers are each capable of producing 30 - $50\ \text{mW}$ of optical power, so arrays of 7 elements or more will produce over $200\ \text{mW}$.

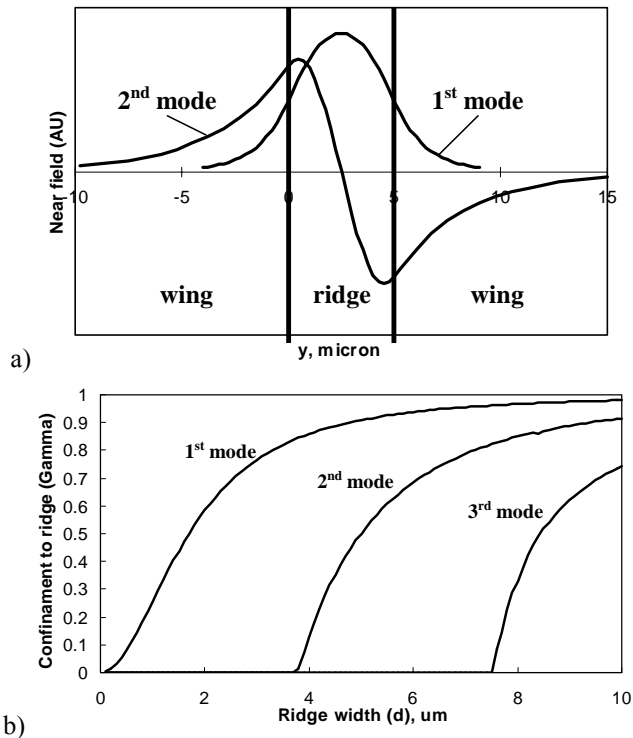


Fig. 3. Modes in the laser. a) mode field shapes in $5\ \mu\text{m}$ thick ridge, b) Confinement to the ridge for different modes (WAVEGUIDE[8] simulations).

IV. LASER DIE THERMAL ANALYSIS

The optimum spacing between the ridges is determined by the distance at which there is insignificant thermal influence on a ridge laser by the heat generated by adjacent ridge lasers. Heat transfer between ridges takes place at two levels 1) in the laser array die and 2) in the laser submount. Below the submount the laser array geometry is of little significance because the submount spreads the heat over a large area.

Since heat conduction is linear, the temperature distribution in a laser array can be found as a superposition of individual ridges. The temperature profile at the quantum well on the facet of a single ridge laser obtained by finite element analysis [10] is given in Fig. 4, assuming the substrate thickness is $100\ \mu\text{m}$, the silicon nitride layer is $0.12\ \mu\text{m}$, the active (heat generating) area thickness is $80\ \text{\AA}$, the ridge width is $5\ \mu\text{m}$, the ridge height is $1\ \mu\text{m}$, the plated gold layer is $1.5\ \mu\text{m}$, the solder layer is $10\ \mu\text{m}$, the laser cavity length is $500\ \mu\text{m}$ and the heat generation is $240\ \text{mW}$ for an optical output of $35\ \text{mW}$. The solder is assumed to cover only $460\ \mu\text{m}$ of the length, with a $20\ \mu\text{m}$ void on each end of the laser.

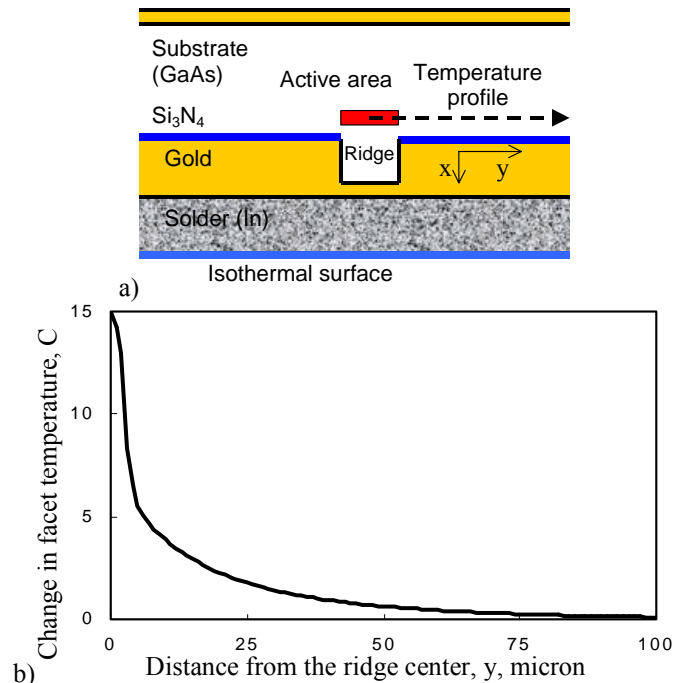


Fig. 4. Finite element analysis of the lateral temperature variation centered on the active layer at the facet of the laser (a) ridge cross-section geometry, b) temperature profile on the laser facet in y direction.

Conventional finite element analysis does not work well for this case since this is a 3-dimensional geometry and the ratio of heat source size to domain size is over 10^4 (a $80\ \text{\AA}$ active layer and a length of $500\ \mu\text{m}$). To perform the analysis with high accuracy within a reasonable time a self-adaptive thermal modeling technique was used [10,11]. The technique uses a nesting method to generate self-adaptive multiple grids. A very fine grid is automatically generated in places with high temperature gradients and a coarser grid is used elsewhere to maintain the same computation accuracy over the domain.

Figure 4 shows that for ridges spaced more than $30\ \mu\text{m}$ apart, thermal crosstalk in the die will be lower than 10% . Thus the array of 7 ridges can be $180\ \mu\text{m}$ wide.

Finally the temperature profile in the array of 10 ridges spaced $67\ \mu\text{m}$ apart is shown in Fig. 5. Each ridge produces $120\ \text{mW}$ of heat. Both Figs. 5a and 5b are obtained by finite element analysis and show only half of the symmetric laser array.

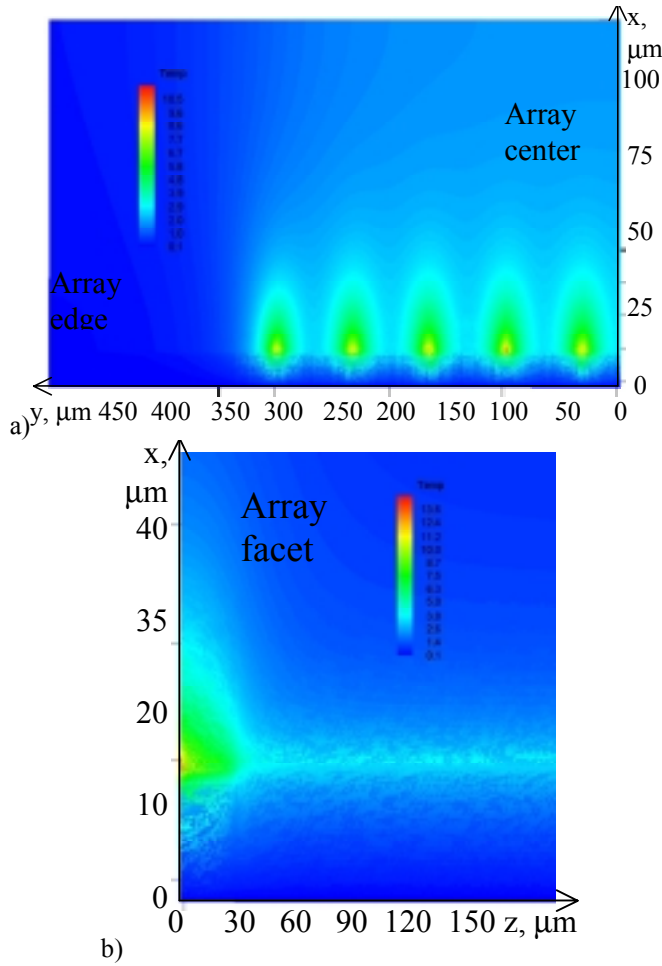


Fig. 5. Temperature field distribution in the laser array die obtained by the finite element analysis, a) the laser facet, b) ridge cross-section.

V. ANALYTIC SOLUTION FOR HEAT TRANSFER IN THE SUBMOUNT

Optimum ridge spacing depends on the properties of the laser die and on the thermal properties of the submount. Although the thermal distribution in the submount can be found by finite element analysis, the submount geometry can be simplified to provide a useful analytical solution by combining two simple geometric models.

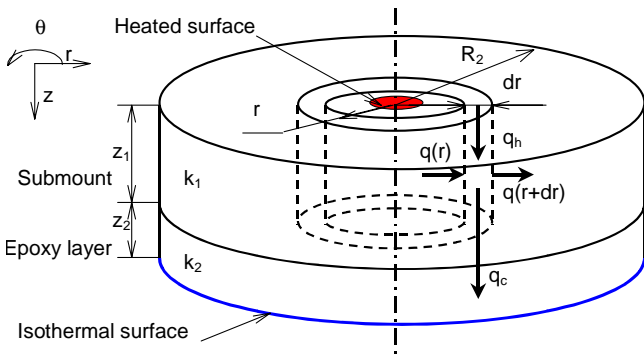


Fig. 6. Cylindrical submount geometry.

Consider a simplified cylindrical submount geometry (Fig. 6) of thickness z_1 , radius R_2 and thermal conductivity k_1 mounted to an isothermal surface with epoxy of thickness z_2 and thermal conductivity k_2 . A small isoflux area of radius R_1 on the top of the submount represents the laser array. The heat flux through the surface is $Q/(\pi R_1^2)$ where Q is the heat generated by the laser array. The other surfaces are assumed to be adiabatic since convection and radiation are negligible. For real submount geometries the following assumptions are usually valid:

$$k_1 \gg k_2, \quad R_1 \ll R_2, \quad z_1/k_1 \ll z_2/k_2, \quad z_1 \ll R_2, \quad z_2 \ll R_2 \quad (3)$$

Due to symmetry the temperature profile will be uniform in the θ direction and the θ component of the heat flux, q_θ , will be zero. Since the thermal conductivity in the submount is much higher than in the epoxy layer, the thermal gradients in the radial direction will be determined by the submount. In the epoxy layer the vertical component of the heat flux is much bigger than the radial component, $q_{r, \text{epoxy}}$, which can be assumed to be zero. Thus there is only a vertical heat flux in the epoxy layer.

In the copper submount we can assume 45-degree heat spreading from the source. Therefore the heat flux will be in the radial direction and the temperature profile depends only on the radius.

The energy balance in a cylindrical element of radius r and thickness dr is given by

$$\begin{aligned} & \left(\begin{array}{c} \text{Energy in} \\ \text{center face} \end{array} \right) + \left(\begin{array}{c} \text{Heat from} \\ \text{isoflux surface} \end{array} \right) = \\ & \left(\begin{array}{c} \text{Energy out} \\ \text{outer face} \end{array} \right) + \left(\begin{array}{c} \text{conduction through} \\ \text{epoxy layer} \end{array} \right) \end{aligned} \quad (4)$$

The energy incident on the inner cylindrical interface $q(r)$ is given by:

$$q(r) = -k_1 2\pi r z_1 \frac{dT(r)}{dr} \quad (5)$$

and the energy exiting the outer cylindrical interface $q(r + dr)$ is given by:

$$\begin{aligned} q(r + dr) &= -k_1 2\pi (r + dr) z_1 \frac{dT(r + dr)}{dr} = \\ &= -k_1 2\pi (r + dr) z_1 \left(\frac{dT}{dr} + \frac{d^2T}{dr^2} dr \right) \end{aligned} \quad (6)$$

The heat from the isoflux surface $q_h(r)$ is given by:

$$q_h(r) = \frac{2\pi Q dr}{\pi R_1^2} h(R_1 - r) \quad (7)$$

where $h(x)$ is a step function (1 for $x > 0$, and zero otherwise).

The conduction through the epoxy layer q_c is given by

$$q_c = \frac{2\pi r k_2 T(r) dr}{z_2} \quad (8)$$

Combining the above equations and dropping the dr^2 term we get:

$$\begin{aligned} & 2\pi r z_1 k_1 \frac{d^2T}{dr^2} dr + 2\pi z_1 k_1 \frac{dT}{dr} dr + \\ & + \frac{2\pi Q dr}{\pi R_1^2} h(R_1 - r) - \frac{2\pi r k_2 T dr}{z_2} = 0 \end{aligned} \quad (9)$$

Equation (9) can be simplified to:

$$\frac{d^2 T}{dr^2} + \frac{1}{r} \frac{dT}{dr} - C_1 T + C_2 = 0, \quad (10)$$

$$\text{where } C_1 = \frac{k_2}{z_1 z_2 k_1}, \quad C_2 = \begin{cases} \frac{Q}{\pi z_1 k_1 R_1^2} & r \leq R_1 \\ 0 & r > R_1 \end{cases}$$

By substituting $x = r\sqrt{C_1}$, $w = T - C_1 / C_2$ equation (10) can be transformed to a Bessel differential equation:

$$\frac{d^2 w}{dx^2} + \frac{1}{x} \frac{dw}{dx} - w = 0 \quad (11)$$

The solution for the Bessel equation is expressed in terms of the modified Bessel functions of zero order $I_0(x)$ and $K_0(x)$:

$$T_1 = \frac{C_2}{C_1} + a_1 I_0(x) + b_1 K_0(x) \quad \text{for } x \leq x_1, \quad x_1 = R_1 \sqrt{C_1} \quad (12a)$$

$$T_2 = a_2 I_0(x) + b_2 K_0(x) \quad \text{for } x > x_1 \quad (12b)$$

Coefficients a_1 , b_1 , a_2 and b_2 can be found from 4 boundary conditions. Requiring zero flux at the edges results in

$$\frac{dT_1(0)}{dx} = 0, \quad \frac{dT_2(x_2)}{dx} = 0, \quad \text{where } x_2 = R_2 \sqrt{C_1}, \quad (13)$$

and requiring continuity of temperature and flux at $x = x_1$ results in

$$T_1(x_1) = T_2(x_1), \quad \frac{dT_1(x_1)}{dx} = \frac{dT_2(x_1)}{dx}. \quad (14)$$

By substituting Eqs. (12) into Eqs. (13) and (14) and solving for a_1 , b_1 , a_2 and b_2 we find:

$$a_1 = \frac{C_2}{C_1} \frac{\alpha}{I_0(x_1)(1-\alpha) + I_1(x_2)K_0(x_1)/K_1(x_2)}, \quad (15a)$$

$$\alpha = 1 - \frac{I_1(x_2)K_1(x_1)}{I_1(x_1)K_1(x_2)},$$

$$b_1 = 0, \quad a_2 = \frac{a_1}{\alpha}, \quad b_2 = a_2 \frac{I_1(x_2)}{K_1(x_2)}. \quad (15b)$$

The temperature along the axis of the cylinder ($r = 0$) is:

$$T_1(0) = \frac{C_2}{C_1} + a_1 \quad (16)$$

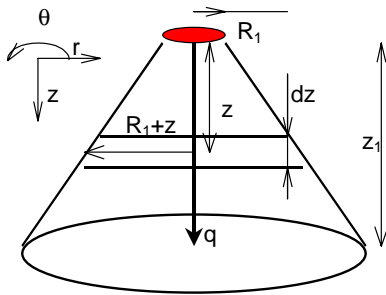


Fig. 7. 45 degree heat spreading model .

To obtain the temperature at the center of the heated surface (the point representing the center of the laser array, P1) we need to add the temperature difference between the top and the bottom of the axis of the submount. Using the standard 45 degree model (Fig. 7):

$$dT = \frac{Q dz}{\pi(R_1 + z)^2 k_1},$$

$$\Delta T = \int_0^{z_1} \frac{Q dz}{\pi(R_1 + z)^2 k_1} = \frac{Q z_1}{\pi k_1 R_1 (R_1 + z_1)} \quad (17)$$

Thus the highest temperature at the center of the laser array is found as a sum of the temperature rises given by the two models from Eqs. (12), (15) and (17):

$$T_{\max} = \frac{Q z_1}{\pi k_1 R_1 (R_1 + z_1)} + \frac{Q z_2}{\pi k_2 R_1^2} \left[1 + \beta \left(R_1 \sqrt{\frac{k_1}{z_1 z_2 k_2}}, R_2 \sqrt{\frac{k_1}{z_1 z_2 k_2}} \right) \right] \quad (18)$$

where

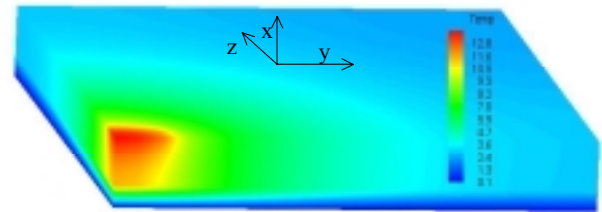
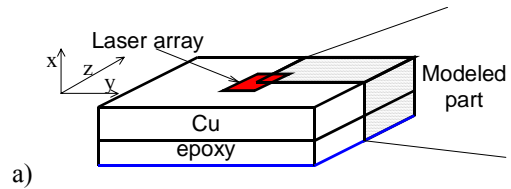
$$\beta(x_1, x_2) = \frac{x_1}{I_1(x_2)} (I_1(x_1)K_1(x_2) - I_1(x_2)K_1(x_1)) \quad (19)$$

In equation (18) the term $Q z_2 / (\pi k_2 R_1^2)$ represents the temperature if the device was placed on epoxy (with an isothermal surface below) without the submount. The β term (which ranges from 0 to -1) represents the temperature reduction introduced by the spreading of the heat in the submount.

Although the laser array and submount are not cylindrical, an equivalent radius R_1 that gives the same area of the heated interface between the laser and the submount, and another radius R_2 equivalent to the area of the submount can be calculated. If we have Δx_L by Δy_L rectangular laser array on a Δx_s by Δy_s submount of thickness z_1 , we can calculate the equivalent radii as follows:

$$R_1 = \sqrt{\Delta x_L \Delta y_L / \pi}, \quad R_2 = \sqrt{\Delta x_s \Delta y_s / \pi} \quad (20)$$

To check the validity of this model, a finite element analysis [10,11] of a laser array with an area of 500 μm by 600 μm and heat generating 2.4W on a 5 mm by 6 mm copper ($k_1 = 398$ W/mK) submount of thickness 0.25mm that is attached to an isothermal surface with either 100 μm of silicone grease ($k_2=2.3$ W/mK) or with 200 μm of thermally conductive epoxy ($k_2=1$ W/mK). The submount geometry used for the finite element analysis and the obtained temperature distribution (for the case of silicone grease) are shown the Fig. 8 and shows that despite the rectangular shape of the submount and the laser array, the resulting temperature profile is roughly cylindrical, as assumed in the analytical model.



b)

Fig. 8. a) Laser submount geometry and b) the temperature distribution in the submount with laser array obtained by finite element analysis.

Excellent agreement of the analytical model with the finite element analysis is shown in Fig. 9. The lines represent analytical calculation using Eqs. (18)-(20) and the diamonds represent the results of the finite element analysis. The thick lines represent calculations for the case of epoxy between the submount and the heatsink and the thin lines represent the case of silicone grease between the submount and the heatsink. The dotted lines are for an ideal submount with the $k=\infty$ and represent the theoretical minimum temperature rise. The analytic model and the finite element analysis agree with 5%, which is close to the error in the finite element analysis (2%).

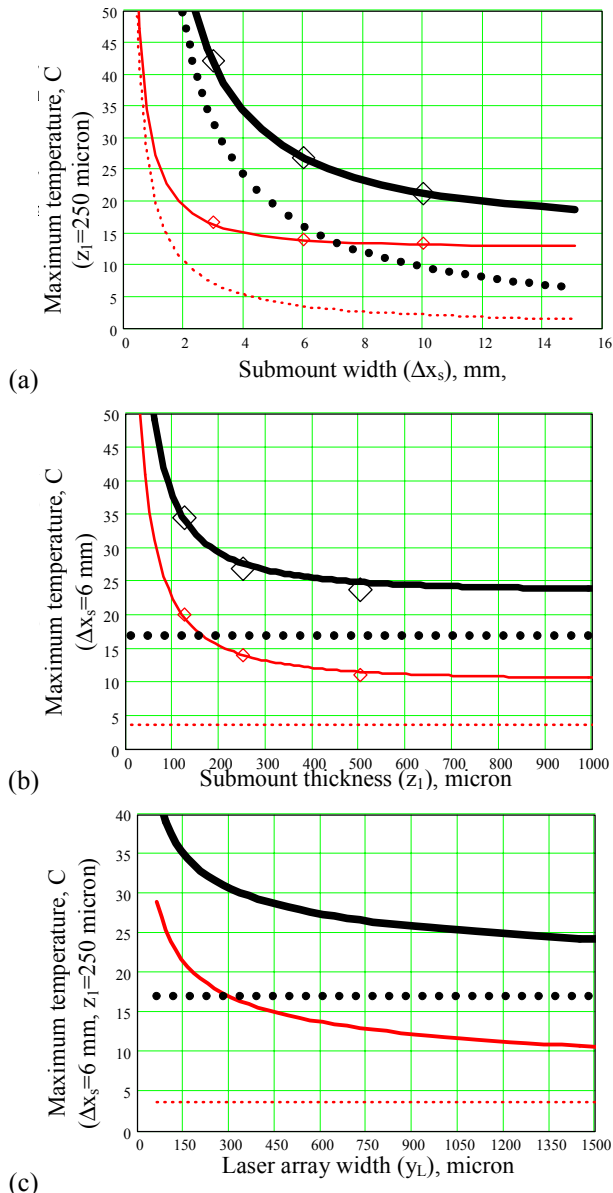


Fig. 9. Maximum temperature rise at the copper submount/laser interface relative to isothermal surface with respect to submount width (a) submount thickness (b) and laser array width (c). The heated surface is 500 by 600 μm . The submount length $\Delta y_s=5\text{mm}$. Thin curves for submounts mounted with 100 μm silicone grease, $k_2=2.3\text{ W/mK}$, thick curves for submounts mounted with 200 μm thermally conductive epoxy, $k_2=1\text{ W/mK}$. Solid lines represent analytical solution, diamonds represent results obtained by the finite element analysis and dotted lines represent results for an ideal submount with $k_1 = \infty$.

Figure 9 can be used to determine the optimum size of the submount and the laser array using the criteria of the minimum temperature rise (at the interface of the copper submount/laser array) and the minimum size of the array and submount. Increasing the submount thickness beyond 250 μm or increasing submount width over 4 mm (silicone grease mounted) or 8 mm (epoxy mounted) will not significantly decrease the temperature rise.

From the theoretical model, the maximum temperature of the heated area can be calculated as a function of the laser array width (with a fixed number of ridges spaced over the width). The results for a 5x6x0.25 mm submount (Fig. 9c) show that for laser arrays with widths smaller than 450-600 μm , the maximum temperature increases rapidly, while increasing the laser array width beyond 600 μm provides little reduction in temperature.

Comparing the thermal analysis data for the laser die and the submount suggests that the optimum array size and ridge spacing is determined mainly by the properties of the submount rather than laser array chip. Although an ideal submount with an infinite thermal conductivity allows a 25 μm ridge spacing (Fig. 4.), realistic submounts require array widths between 450 to 600 μm to effectively dissipate heat. This means that for a 7-ridge array, the ridge spacing should be increased to 70 to 100 μm where thermal cross talk is negligible (< 1%).

The actual temperature in the quantum well of the laser array is found by adding the temperature values from Fig. 5 (the temperature rise in the array and solder) to the heatsink temperature increase (Fig. 9b), in the submount and silicone grease, added to the temperature of the heatsink.

For a 600 by 500 μm laser array producing 2.4 W of heat that is soldered to a 5 mm by 6 mm by 0.25 mm copper submount that is attached to a heatsink by 100 μm of silicone grease (thermal conductivity 2.3 W/mK), the temperature rise from the laser facet to the heat sink will be 29°C, of which 15°C is the temperature rise in the laser array and solder and 14°C is the temperature rise in the submount and silicone grease.

VI. RWG LASER ARRAY TESTING

The RWG laser arrays (Fig. 2) were fabricated with the epitaxial structure listed in Table 1. Two different wafers were used. B779 has a central wavelength of 636 nm and a threshold current density of 430A/cm². B765 has a 634 nm wavelength and a threshold current density of 400A/cm².

The testing results for single RWG lasers from both materials show the same slope (dL/dI) of 0.8 mW/mA per facet, and threshold currents of 31- 41mA (B779) and 25- 31mA (B765).

The slope is very close to the predicted value of 0.8753 mW/mA, although the value of the threshold current is 50% higher than predicted, 27 mA and 37mA compared to 21.7 mA. A possible explanation for the increased threshold current is larger than expected current spreading, which is supported

by the observation that the threshold current does not depend on ridge width.

The maximum CW power for the single RWG lasers is 18-20 mW per facet (35-40 mW total) before rapid degradation.

Laser arrays with different number of ridges were fabricated from the same materials summarized in Table 3. Pulsed (1 microsecond pulses and 0.1% duty cycle) L-I and V-I curves at a temperature of 15 C for these ridge wave-guide arrays are shown in Fig. 10.

TABLE III
LASER ARRAYS TESTING SUMMARY

Material	B76	B76	B76	B77	B77	B765
	5	5	5	9	9	
# of ridges in array	3	7	10	10	20	Broad area
Threshold current, mA	65	135	170	310	570	260
Slope per facet, mW/mA	0.52	0.45	0.49	0.47	0.41	0.41
Differential resistance, Ohm	12	6	6.5	3	2	1.6
Maximum CW current, mA	-	340	400	550	-	330
Max. output CW power, mW/facet	-	90	100	125	-	27
Maximum efficiency at CW, %	-	10	10.6	10.8	-	5.3

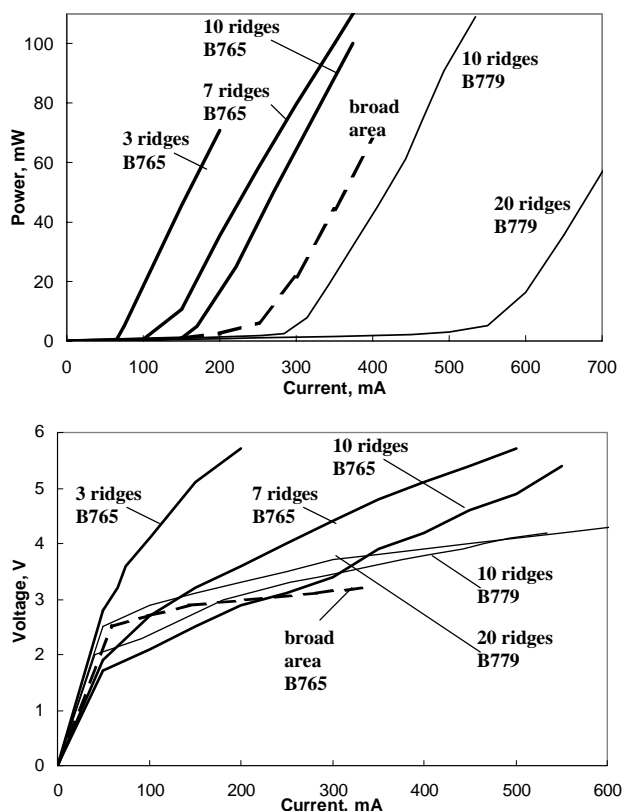


Fig. 10. Pulsed L-I and V-I curves (1 microsecond pulses and 0.1% duty cycle at a temperature of 15 C).

The threshold currents in RWG arrays are 25 - 40% lower than the threshold current of a single RWG multiplied by the number of ridges. Additionally, the slope of the L-I curve in RWG arrays is 30 - 40% lower than in single RWGs. This may

be because the ridges in the array may have slightly different resistances allowing higher than average current in some ridges resulting in early onset of lasing (in some ridges). The ridges that turned on later than the others produce less light but still consume considerable current and therefore cause a lower slope. The difference in output power of different ridges can be seen in Fig. 11 where ridges 1, 5, 6, and 10 (counting from the top) produce much more light than ridges 4, 8, 9.



Fig. 11. Lasing 10 element RWG array.

This non-uniformity in ridge performance within the array has negligible effect on the spectrum. For most devices, the spectrum of RWG arrays, shown in Fig. 12, is almost identical to the spectrum of single RWG lasers. The small spectral broadening in arrays (from 0.3-0.6 nm to 0.5-1 nm) has no effect in our application, especially considering that there is a ± 1 nm central wavelength variation for devices made from the same wafer.

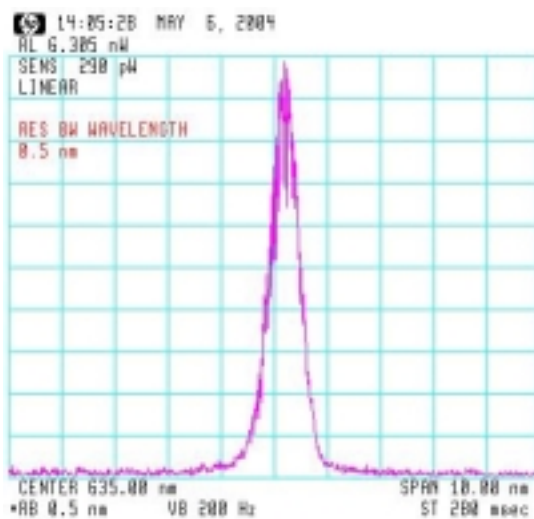


Fig. 12. Typical spectrum of a RWG array of 10 ridges

The highest CW power was achieved for RWG arrays of 7 or 10 ridges. The devices fabricated from wafer B765 require less current to achieve high power than devices from wafer B779. However, due to n-metal problems, devices from wafer B765 have much higher resistances and operating voltage than those from wafer B779. As a result, B779 RWG arrays of 10 ridges can achieve higher powers and were used in early prototypes.

Arrays of 7 and 10 ridges from wafer B765 are expected to have much higher performance when the contact problem is corrected.

Despite the high voltage problem, these laser arrays show much better CW performance than 100 μm wide broad area lasers made of the same material. Broad area lasers with lower operation currents and lower voltage still generate heat in a very small area that leads to device degradation. Although these RWG arrays produce almost twice the heat, it is spread over a six times larger area, allowing four times more output.

VII. SCATTERING ELEMENTS AND FACET COATINGS

Unlike most lasers applications, a very broad radiation pattern is desired for the lasers used in balloon catheters for Photodynamic Therapy. Such illumination patterns can be achieved by applying optical scattering elements to the facets of semiconductor lasers as shown in Fig.13. These scattering elements, consisting of a light transparent polymer (refractive index ~ 1.51) with nanoparticles, will affect the reflectivity, and thus the threshold and power output of the lasers.

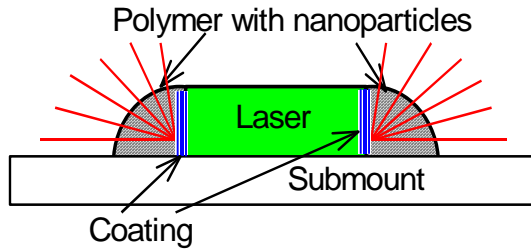


Fig. 13. Edge-emitting 635nm laser on a Cu submount with a scattering element

The intensity reflectivity R at the interface between two media with refractive indexes n_1 and n_2 is:

$$R = \left(\frac{n_2 - n_1}{n_2 + n_1} \right)^2 \quad (21)$$

The effective refractive index of the laser structure (n_{eff}) found by MODEIG software [8] is 3.286 so the reflectivity at the air interface is $R = 28.4\%$. If the laser facet is embedded in a polymer with an index of 1.51, the reflectivity R is 13.7%, causing increased threshold current and decreased laser efficiency.

Such drastic changes can be avoided by using a multilayer facet coating designed to provide a facet reflectivity of $\sim 35\%$ in both air and polymer, allowing the laser to perform the same with or without scattering elements.

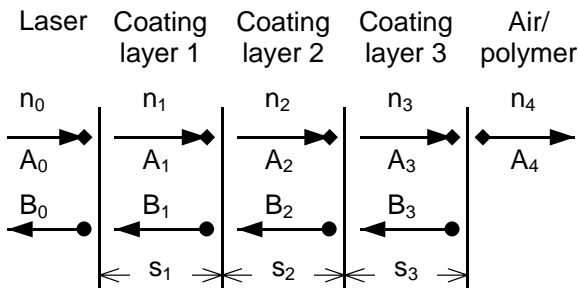


Fig. 14. 3-layer coating schematic

Figure 14 illustrates a 3-layer coating between a laser and either air or polymer. In the i th layer of an N -layer coating, A_i represents a forward traveling wave, B_i represents a backward traveling wave, s_i is the layer thickness, and n_i is the refractive index of the layer. The $(N+1)$ th layer is the outside media (air or polymer) and since the light is incident from the laser, $B_{N+1} = 0$ and n_{N+1} is either 1 (air) or 1.51 (polymer). Layer 0 is the laser so $n_0 = n_{\text{eff}}$. The reflectivity R seen at the laser-coating interface is $(B_0/A_0)^2$, which is found by summing the amplitudes and phases of the fields reflected at each interface in the multilayer stack. The field reflectance ρ_i at the boundary between the i th and $i+1$ th layer is:

$$\rho_i = \frac{n_i - n_{i+1}}{n_i + n_{i+1}} \quad (22)$$

and the sum of the backward traveling waves at each interface (at each dot in Fig. 14) is

$$B_i = A_i \rho_i + B_{i+1} \exp(2\pi j s_{i+1}) \sqrt{1 - \rho_i^2} \quad (23)$$

and the sum of the forward traveling waves at each interface (at each diamond in Fig. 14) is

$$A_i = A_{i-1} \exp(2\pi j s_i) \sqrt{1 - \rho_{i-1}^2} - B_i \exp(4\pi j s_i) \rho_{i-1} \quad (24)$$

where $j = \sqrt{-1}$.

The reflectivity of all layers after layer i is:

$$r_i = \frac{B_i}{A_i} \quad (25)$$

Substituting A_i from Eq.(24) into Eq.(25) results in

$$B_i = A_i r_i = r_i A_{i-1} \exp(2\pi j s_i) \sqrt{1 - \rho_{i-1}^2} - r_i B_i \exp(4\pi j s_i) \rho_{i-1} \quad (26)$$

which reduces to

$$B_i = A_i r_i = \frac{r_i A_{i-1} \exp(2\pi j s_i) \sqrt{1 - \rho_{i-1}^2}}{1 + r_i \exp(4\pi j s_i) \rho_{i-1}} \quad (27)$$

From Eq.(23) with i changed to $i-1$ we find

$$B_{i-1} = A_{i-1} \rho_{i-1} + B_i \exp(2\pi j s_i) \sqrt{1 - \rho_{i-1}^2} \quad (28)$$

Substituting Eqs. (25) and (27) (changing i to $i-1$), into (28) results in

$$A_{i-1} r_{i-1} = A_{i-1} \rho_{i-1} + \frac{r_i A_{i-1} \exp(2\pi j s_i) \sqrt{1 - \rho_{i-1}^2}}{1 + r_i \exp(4\pi j s_i) \rho_{i-1}} \exp(2\pi j s_i) \sqrt{1 - \rho_{i-1}^2} \quad (29)$$

which can be simplified to obtain a formula for r_{i-1} :

$$r_{i-1} = \frac{r_i + \rho_{i-1} \exp(-4\pi j s_i)}{\exp(-4\pi j s_i) + r_i \rho_{i-1}} \quad (30)$$

where $r_N = \rho_N$ is the reflectivity (Eq. 22) at the last interface and the reflectivity seen by the laser is $R = |r_0|^2$, which is found by an iterative solution of Eq.(30) with i ranging from N to 1.

Silicon dioxide ($n = 1.5$) and titanium dioxide ($n = 2.43$) are high index contrast coatings that have low losses at 635 nm.

To obtain the maximum coating reflectivity, the SiO_2 layer should be adjacent to the laser so that the maximum index contrast is obtained. Starting with the maximum reflectivity, R can be reduced by adjusting the thicknesses of each coating layer. Although two layers are sufficient to obtain $R = 35\%$ for the specified coatings, a three-layer coating is less sensitive

to index and thickness variations and results in a larger solution space. The resulting three-layer coating on the laser ($n_0 = 3.286$) facets consists of 1) SiO_2 ($n_1 = 1.5$), 2) TiO_2 ($n_2 = 2.43$), 3) SiO_2 ($n_3 = 1.5$) followed by air ($n_4 = 1$) or by polymer ($n_4 = 1.51$).

The coating reflectivity R is a function of the coating layers thicknesses s_1, s_2, s_3 and the outside media refractive index:

$$R = f(s_1, s_2, s_3, n_4) \quad (31)$$

The specified target reflectivity of $R=35\%$ in both air and polymer is achieved by selecting layers thicknesses s_1, s_2, s_3 that satisfy:

$$R(s_1, s_2, s_3, 1.5) = 0.35 \quad (32a)$$

$$R(s_1, s_2, s_3, 1) = 0.35 \quad (32b)$$

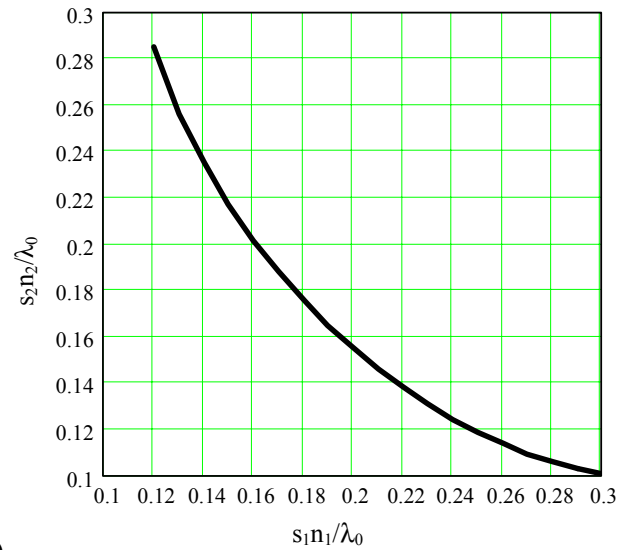
The boundary between SiO_2 and polymer will not reflect since they have the same refractive index. Therefore s_3 will have no effect in polymer media and Eq.(32a) can be simplified:

$$R(s_1, s_2, 1.5) = 0.35 \quad (33)$$

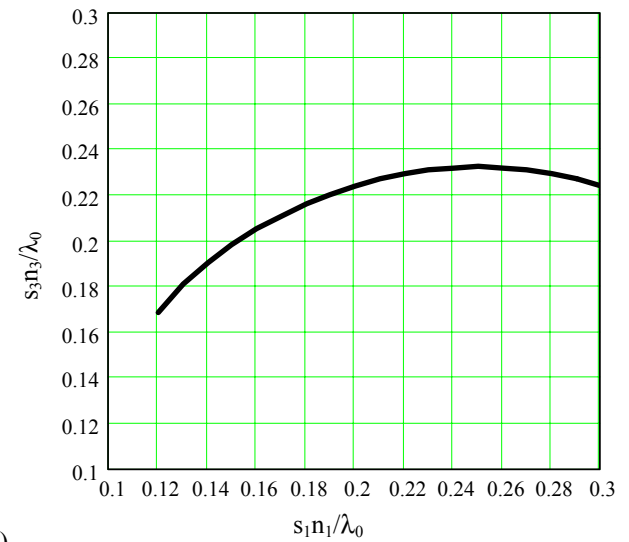
The normalized thickness $s_2 n_2 / \lambda_0$ (where $\lambda_0 = 635$ nm is the free space wavelength) is plotted in Fig. 15a as a function of $s_1 n_1 / \lambda_0$ by solving Eq. (33) Eq (32b) can now be written as:

$$R(s_1, s_2(s_1), s_3, 1) = 0.35 \quad (34)$$

and can be solved for s_3 as a function of s_1 ($s_3 = s_3(s_1)$), (Fig.15b). Note that Eqs.(33) and (34) will have multiple periodic solutions with period 0.5, because $\exp(-4\pi j s_i)$ is a periodic function of s_i . We are interested in minimizing the coating thicknesses to reduce diffractive losses (which have been neglected).



a)



b)

Fig. 15. Solutions for layers thickness

Figure 15 represents a set of solutions for the coating thicknesses. By choosing s_1 in the range of 0.12 to 0.3 we can select s_2 (Fig. 15a) and s_3 (Fig. 15b) so that the target reflectivity R is 35% in both air and in polymer.

The coating layer thickness tolerance is typically 5 to 10% and the tolerance on the refractive indices of the layers is $\sim 0.5\%$. These variations result in a range (minimum and maximum values) of reflectivities as shown in Fig. 16. Figure 16 indicates that the minimum reflectivity variations are at s_1 equal to 0.26 or 0.12. The reflectivity variations at these points are below 3% compared to $\sim 4\%$ at other points. The coating parameters for $s_1 = 0.13$ (Table 4) were applied to the AlGaInAs lasers described in Section 3.

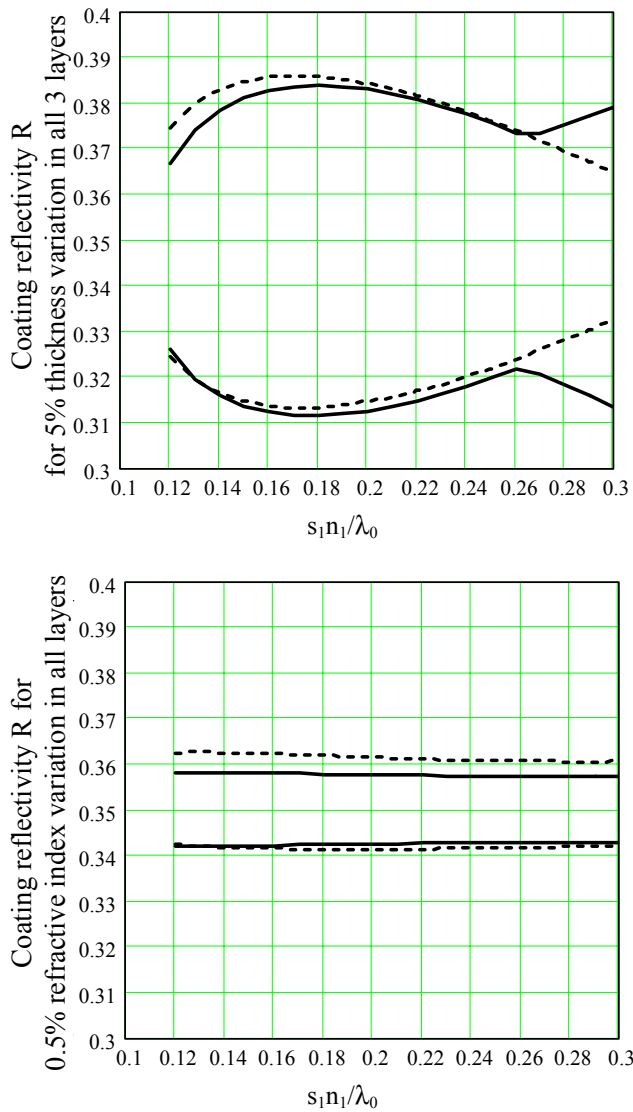


Fig. 16. Coating reflectivity R variation for 5% thickness variation in all 3 coating layers and for 0.5% refractive index variation in all layers including laser. Top and bottom curves represent min and max values of reflectivity. Solid line represents reflectivity in air, dashed line for polymer.

TABLE IV
A COATING DESIGN

Layer	Laser	Coating layer#1	Coating layer#2	Coating layer#3	Media
Material	AlGaInP/ GaAs	SiO ₂	SiO ₂	SiO ₂	Air/ polymer
Refractive index	3.286	1.5	2.43	1.5	1 / 1.51
Thickness, λ		0.13	0.255	0.18	
Thickness, nm		55	67	76	

VIII. CONCLUSIONS

A 635 nm ridge waveguide laser array was designed and optimized for better heat extraction allowing higher power and improved reliability compared to broad area lasers fabricated from the same material.

An analytical formula for heat transfer in the laser array and the submount showed good agreement with results obtained by finite element analysis.

These ridge waveguide arrays produce greater than 3 times more optical power from 7 to 10 ridges (each 5 μm wide) than 100 μm wide broad area lasers because the heat is spread over a larger area.

Although the output power from these laser arrays was limited to 200 mW because of high contact resistivity, more than 400 mW is expected with proper contacts.

REFERENCES

- [1] J. Van den Boogert, R. van Hillegersberg, H.J. van Stavereen, et al., "Timing of illumination is essential for effective and safe photodynamic therapy: a study in the normal rat esophagus," in *Br J Cancer* 79(5-6), 825-30 (1999).
- [2] B.J. Tromberg, A. Orenstein, S. Kimel, S.J. Barker, J. Hyatt, J.S. Nelson, M.W. Berns, "In vivo tumor oxygen tension measurements for the evaluation of the efficiency of photodynamic therapy," in *Photochem Photobiol* 52, 375-385 (1990).
- [3] S.L. Jacques, "Laser-tissue interactions: photochemical, photothermal, and photomechanical mechanisms," in *Surgical Clinics of North America*, 72, 531-558 (1992).
- [4] A. Rosen, H. Rosen, "Catheter with Distally Located Integrated Circuit Radiation Generator". US Patent Number 4,998,932, March 1991
- [5] R.A. Hsi, A. Rosen, C. Rodriguez, "Method and Apparatus for Catheter Phototherapy with Dose Sensing". Patent Pending, Docket No. 367, November 12, 1999.
- [6] A. Rosen, H. Rosen, Editors, *New Frontiers in Medical Device Technology* (John Wiley and Sons, pages 95-98).
- [7] High power devices, Inc, <http://www.hpding.com/>
- [8] R. Smith, G. Mitchell, "Calculation of complex propagating models in arbitrary, plane layered, complex dielectric structures", University of Washington, Seattle, WA, EE Technical report No. 206, Dec. 1977. A PC version is available at <http://www.seas.smu.edu/modeig/>.
- [9] D.P. Bour, R.S. Geels, D.W. Treat, T.L. Paoli, F.Ponce, R.L. Thorton, B.S. Crusor, R.D. Bringans, and D.F. Welch, "Strained Ga_xIn_{1-x}P/(AlGa)_{0.5}In_{0.5}P Heterostructures and Quantum-Well Laser Diodes". *IEEE Journal of Quantum Electronics*, Vol 30, N2, 593-607, Feb. 1994.
- [10] Raad, P.E., J.S. Wilson, and D.C. Price, "Adaptive Modeling of the Transients of Sub-Micron Integrated Circuits". *IEEE Transactions on Components, Packaging, and Manufacturing Technology - Part A*, Vol. 21, No. 3, September 1998.
- [11] Raad, P., J. Wilson, and D. Price, "System and Method for Predicting the Behavior of a Component," U.S. Patent No. 6,064,810, Issued May 16, 2000.
- [12] B. Chance, M. Cope, E. Gratton, N. Ramanujam, and B. Tromberg "Phase measurement of light absorption and scatter in human tissue" *Review of Scientific Instruments* Vol 69(10) pp. 3457-3481. October 1998

[13] D. P. Bour, and A. Rosen, "Optimum cavity length for high conversion efficiency quantum well diode lasers", *Journal of Applied Physics*, vol. 66, No 7, pp. 2813-2818, Oct 1989

[14] T. M. Chou, "GAIN program", Available at <http://enr.smu.edu/ee/smuphotonics/Gain.htm>



Ivan Charamisinou was born on June 2, 1975 in Minsk, Belarus. Got B.S. and M.S. degree in electrical engineering from the Belarusian State University of Informatics and Radioelectronics in Minsk in 1997.

Currently he is a PhD student at the mechanical engineering department of Southern Methodist University in Dallas, TX. The areas of scientific interests are biomedical engineering, light delivery systems for photodynamic therapy, optoelectronic packaging, precise laser soldering, high power red laser design and fabrication, light scattering theory.



Gemunu S. Happawana is Assistant Professor of Department of Mechanical Engineering, Southern Methodist University (SMU), Dallas, Texas. His degrees: BS (1984, Mathematics, University of Colombo, Sri-Lanka, with honor), MS (1988, Mathematics, Purdue University), Ph.D. (1994 Mechanical Engineering, Purdue University). Since 1989 to 1994 at Purdue University, West Lafayette, Indiana, his research focused on modeling, stability analysis, and control of gas turbine engines,

including vibration effects in mistuned linear and cyclic propulsion systems while working as a research assistant. Since 1995, he has been working in dynamic modeling, analysis and design of multi wheel drive vehicles, and robust multivariable control of nonlinear systems. He is also working in the optoelectronic packaging area of thermal, mechanical, and optical design aspects. Publications: More than 35-Journal and conference papers. Affiliations: SAE (member), ASME (member), OSA (member).



Gary A. Evans was born in Omak, Washington in 1948 and received the BSEE (1970) from the University of Washington and an MSEE (1971) and PhD (1975) from the California Institute of Technology. He taught at the University of Washington and worked at the Aerospace Corporation and TRW before joining the David Sarnoff Research Center (formerly RCA Laboratories) in 1984. Since 1992 he has been a Professor of Electrical Engineering at Southern Methodist

University. Dr. Evans is a licensed professional engineer and has served on numerous professional committees. He is an associate editor of the IEEE *Journal of Quantum Electronics*, co-edited the Academic Press book *Surface Emitting Semiconductor Lasers and Arrays*, and has coauthored over 170 journal and conference publications. He was elected a Fellow of the IEEE for contributions to the development, fabrication, and understanding of semiconductor lasers.



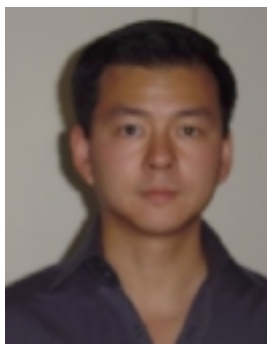
David Bour is an Agilent Fellow in the Photonics and Electronics Research Laboratory at Agilent Laboratories, in Palo Alto, CA, where he is working on the epitaxial growth of semiconductor lasers by metalorganic chemical vapor deposition. From 1991-1999 he was a Principal Scientist in the Electronic Materials Laboratory of the Xerox Palo Alto Research Center, fabricating nitride blue laser diodes and phosphide red laser diodes for laser printing. From 1987-1991 he was a Member of Technical Staff at Sarnoff Corporation. He received a B.S. degree in Physics from MIT in 1983, and a Ph.D. degree in Electrical Engineering from Cornell University in 1987. David was elected a Fellow of the IEEE in 2000, for contributions to the growth and understanding of quantum well lasers.



He currently holds an appointment as Academy Professor of Biomedical and Electrical Engineering in the School of Biomedical Engineering, Science and Health Systems at Drexel University, where he has also held an appointment as Adjunct Professor in the Department of Electrical and Computer Engineering since 1981. He also holds the title of Associate in Medicine at Jefferson Medical College, where he has been engaged in research in the Division of Cardiology since 1970. He has authored more than 150 technical papers, co-edited *High-Power Optically Activated Solid-State Switches* (Norwood,

MA: Artech House, 1993), and *New Frontiers in Medical Device Technology* (New York: Wiley, 1995), as well as six book-chapters in the field of engineering and medicine. He holds over 50 U.S. patents in the fields of engineering and medicine.

Dr. Rosen was elected a Member of National Academy of Engineering, "For contributions to microwave and laser technologies and the medical applications of these technologies." (2002). He was IEEE Distinguished Microwave Lecturer from 1997 to 2000, during which time he has had the opportunity to present his and others' work in the U.S., Japan, Europe and the Middle east. He has received numerous awards, most recently, the IEEE Third Millennium Medal (January 2000) and an IEEE Microwave Award (June 2000). He was the recipient of several RCA and Sarnoff Laboratories outstanding achievement and other professional awards, a 1989 IEEE Region One Award, and a 1997 Drexel University College of Engineering, Electrical and Computer Engineering Department Distinguished Alumni Award.



Alex R Hsi is a Adjunct Assistant Professor, Dept. of Radiation Oncology, Univ. of Pennsylvania. His degrees: BA (1987, Chemistry, Kalamazoo College) and MD (1991, University of Michigan Medical School). From 1997 he was a Clinical Instructor of Dept. of Radiation Oncology, Univ. of Pennsylvania. From 1997 he was

Assistant Professor of Dept. of Radiation Oncology, Univ. of Pennsylvania, from 2003 he is Section Head of Section of Radiation Oncology, Virginia Mason Medical Center. He holds the following awards Best Doctors in Puget Sound, Checkbook.org (Consumer Information & Services Resource, Center for the Study of Services), 2003, Galen's Medical Society Resident Teaching Award, 1993, and Phi Beta Kappa Honor Society, 1987.

TABLE I
MATERIAL COMPOSITION OF EPI STRUCTURE[9]

#	Layer name	635 nm Epitaxial Structure Material	Actual/Ideal Thickness, um
1	P+cap	GaAs	0.05
2	Barrier reducer	Ga _{0.5} In _{0.5} P	0.075
3	p-cladding	Al _{0.5} In _{0.5} P	0.75
4	Etch stop	Ga _{0.6} In _{0.4} P	0.004
5	p-spacer	Al _{0.5} In _{0.5} P	0.25
6	SCH	(Al _{0.6} Ga _{0.4}) _{0.5} In _{0.5} P	0.1063/0.09
7	QW	Ga _{0.5} In _{0.5} P	0.0080
8	SCH	(Al _{0.6} Ga _{0.4}) _{0.5} In _{0.5} P	0.1063/0.09
9	n-cladding	Al _{0.5} In _{0.5} P	1
10	Substrate	GaAs	~100

TABLE II
COMPARISON OF A REAL LASER STRUCTURE
TO IDEAL OPTIMIZED

	As Grown (theory)	Ideal (theory)	Mea- sured
quantum well confinement factor Γ	3.0289%	3.0558%	-
perpendicular far- field divergence	40.0°	41.5°	42°
near-field width	0.2284	0.2181	-
threshold current J_{th}	21.7 mA	21.3 mA	27-41mA

TABLE III
LASER ARRAYS TESTING SUMMARY

Material	B765	B765	B765	B779	B779	B765
# of ridges in array	3	7	10	10	20	Broad area
Threshold current, mA	65	135	170	310	570	260
Slope per facet, mW/mA	0.52	0.45	0.49	0.47	0.41	0.41
Differential resistance, Ohm	12	6	6.5	3	2	1.6
Maximum CW current, mA	-	340	400	550	-	330
Max. output CW power, mW/facet	-	90	100	125	-	27
Maximum efficiency at CW, %	-	10	10.6	10.8	-	5.3

TABLE IV
A COATING DESIGN

Layer	Laser	Coating layer#1	Coating layer#2	Coating layer#3	Media
Material	AlGaInP/ GaAs	SiO ₂	SiO ₂	SiO ₂	Air/ polymer
Refractive index	3.286	1.5	2.43	1.5	1 / 1.51
Thickness, λ		0.13	0.255	0.18	
Thickness, nm		55	67	76	

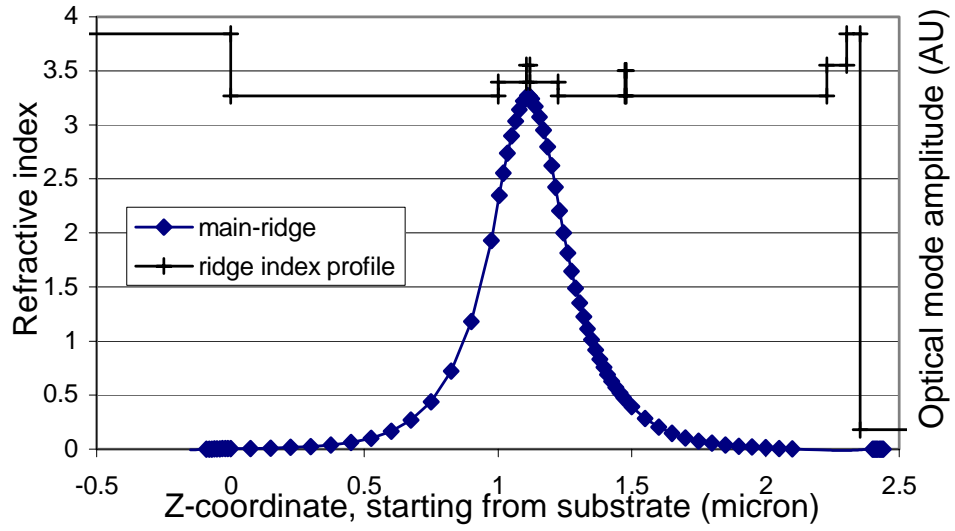


Fig. 1. Index profile and near-field of the as grown structure (Table 1).

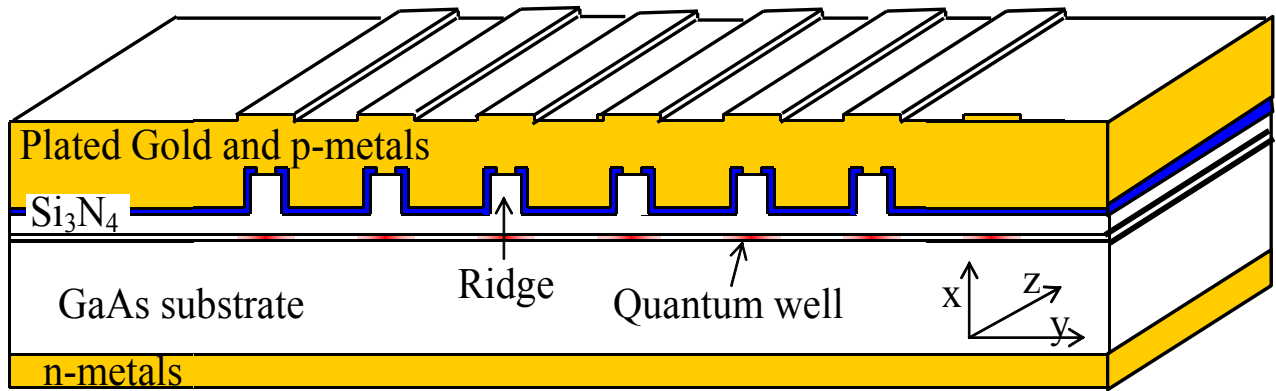


Fig. 2. Laser array

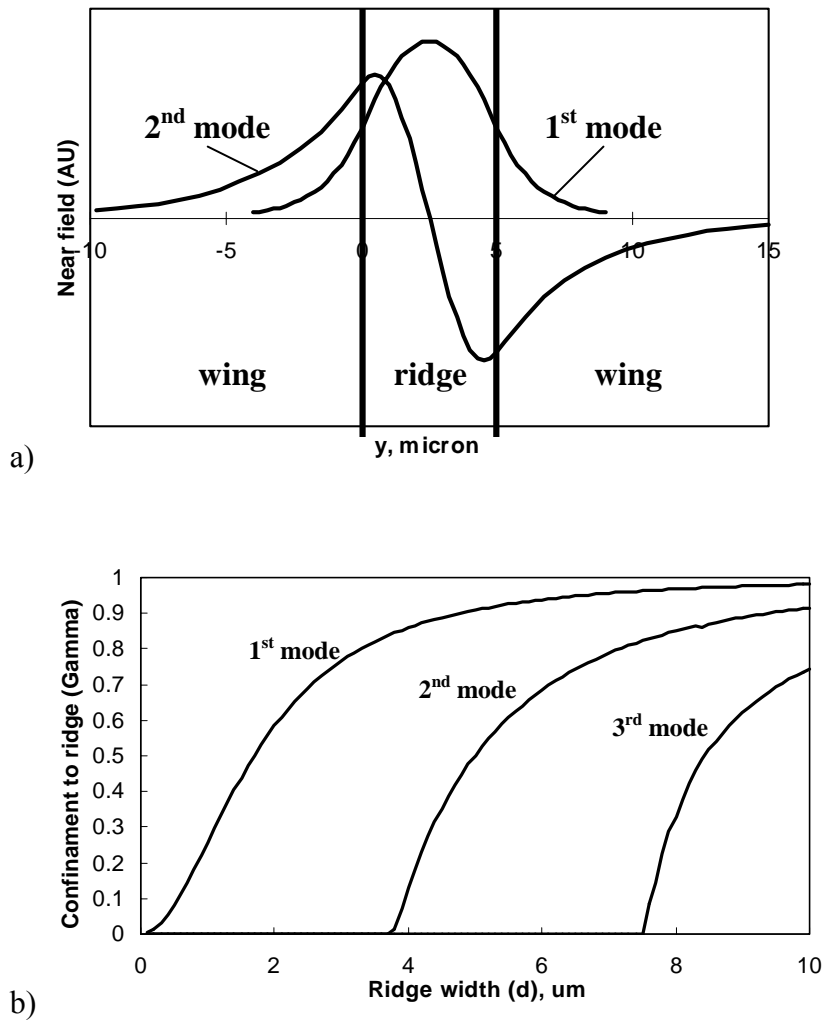


Fig. 3. Modes in the laser. a) mode field shapes in 5 μm thick ridge, b) Confinement to the ridge for different modes (WAVEGUIDE[8] simulations).

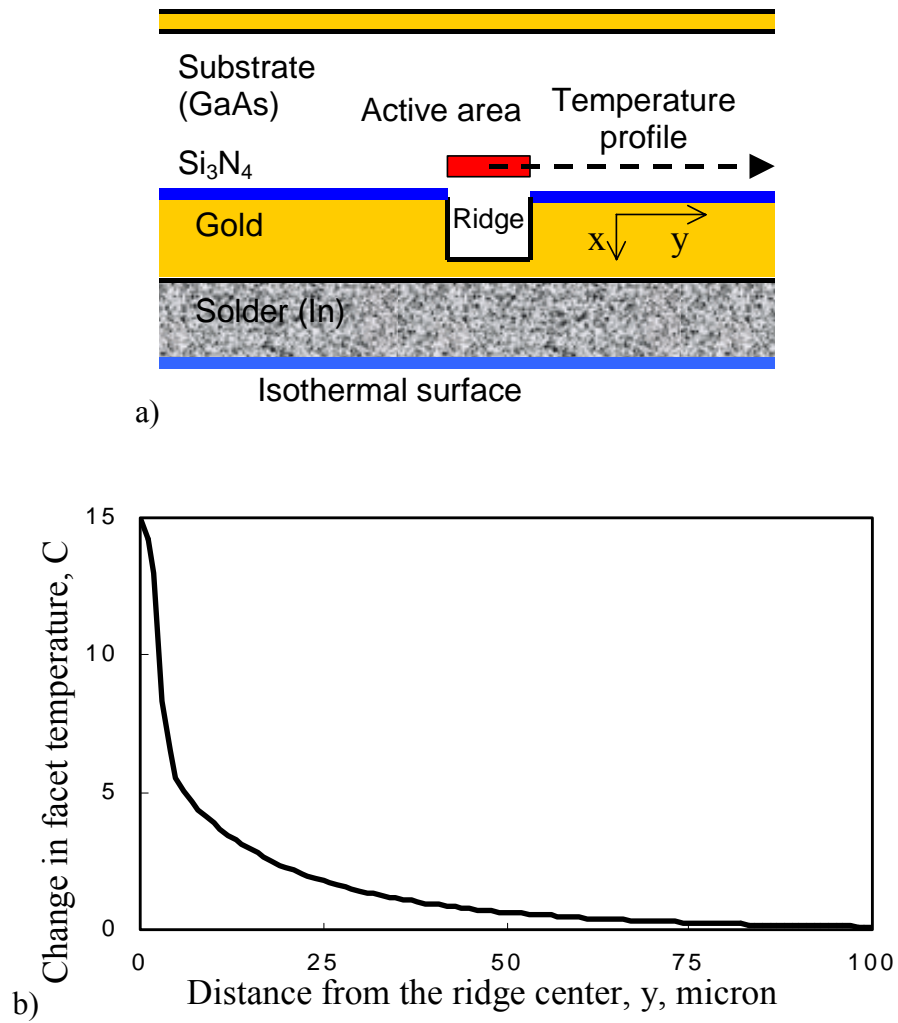


Fig. 4. Finite element analysis of the lateral temperature variation centered on the active layer at the facet of the laser (a) ridge cross-section geometry, b) temperature profile on the laser facet in y direction.

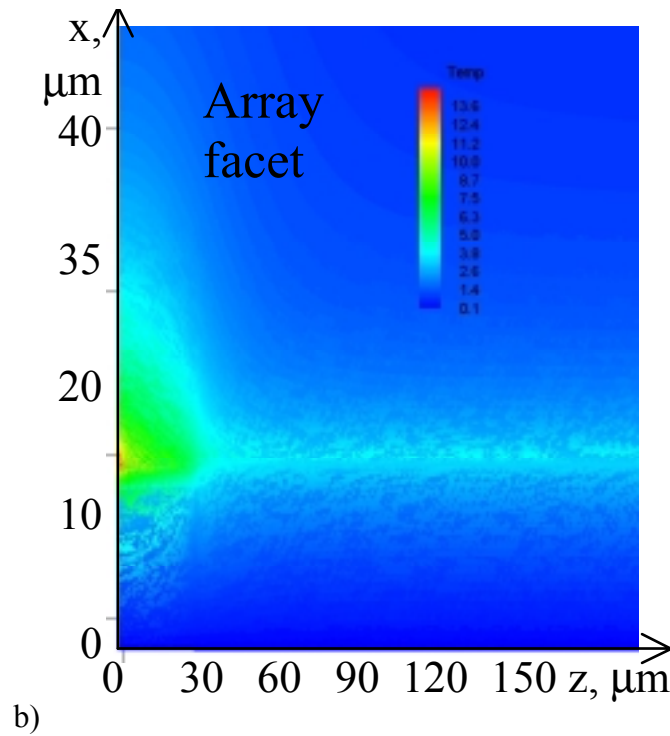
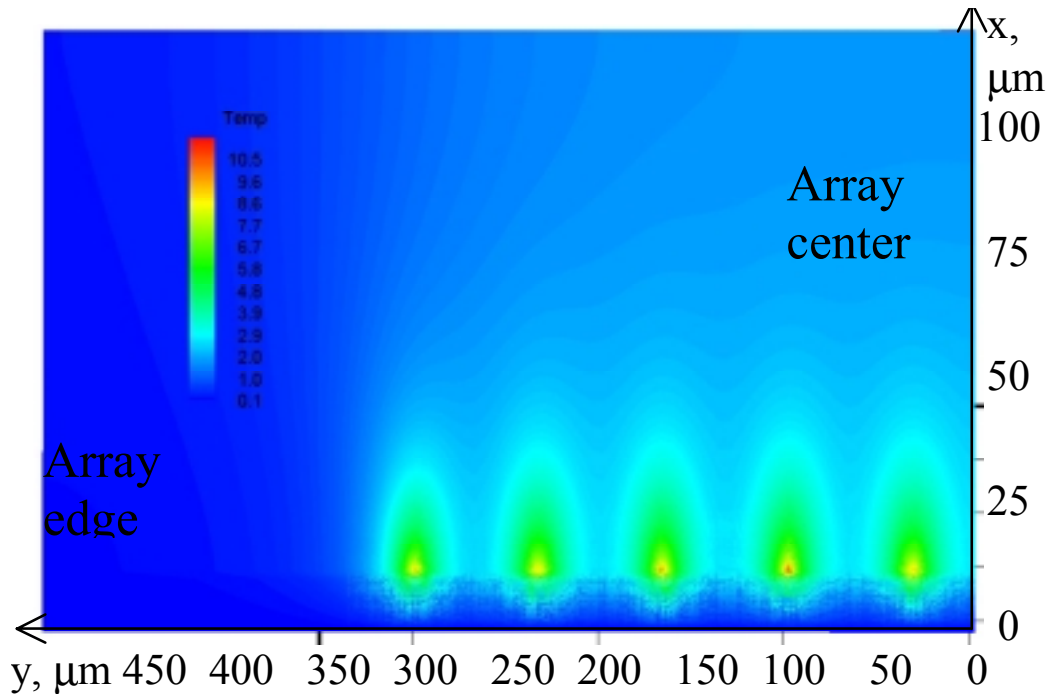


Fig. 5. Temperature field distribution in the laser array die obtained by the finite element analysis, a) the laser facet, b) ridge cross-section

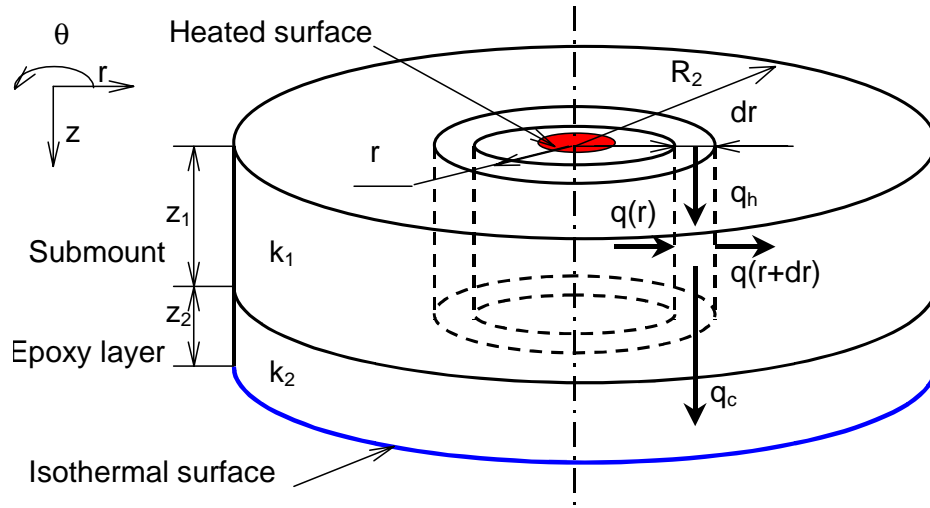


Fig. 6. Cylindrical submount geometry.

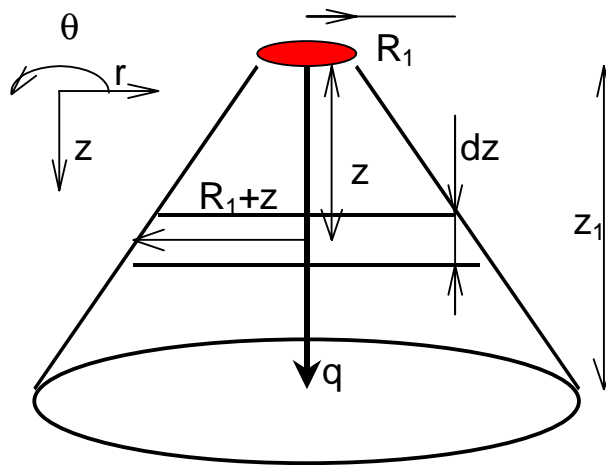


Fig. 7. 45 degree heat spreading model

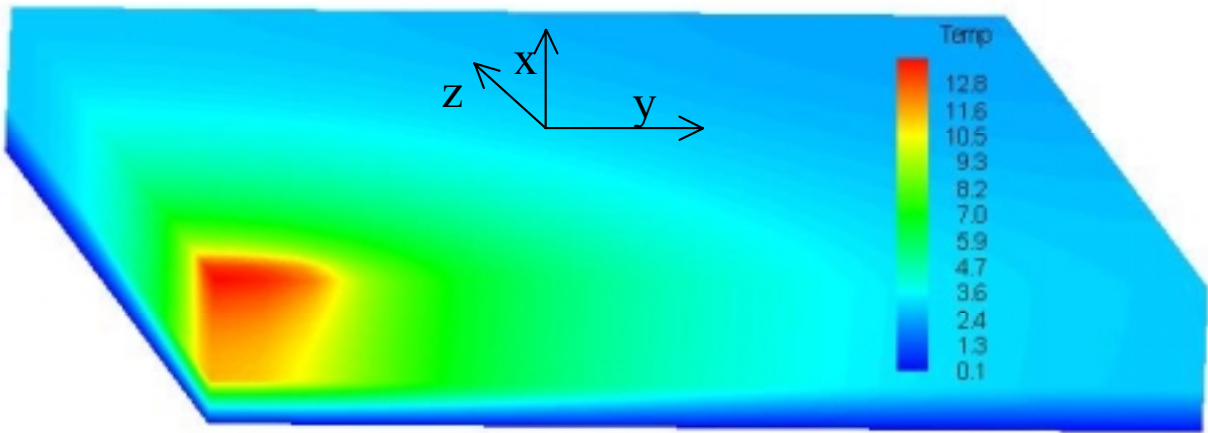
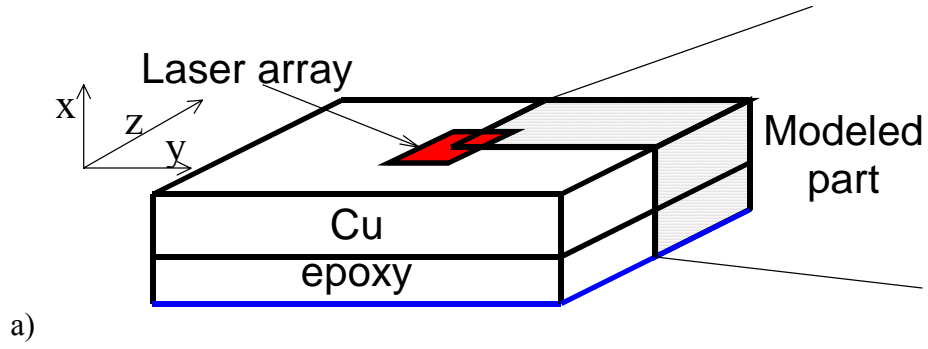


Fig. 8. a) Laser submount geometry and b) the temperature distribution in the submount with laser array obtained by finite element analysis.

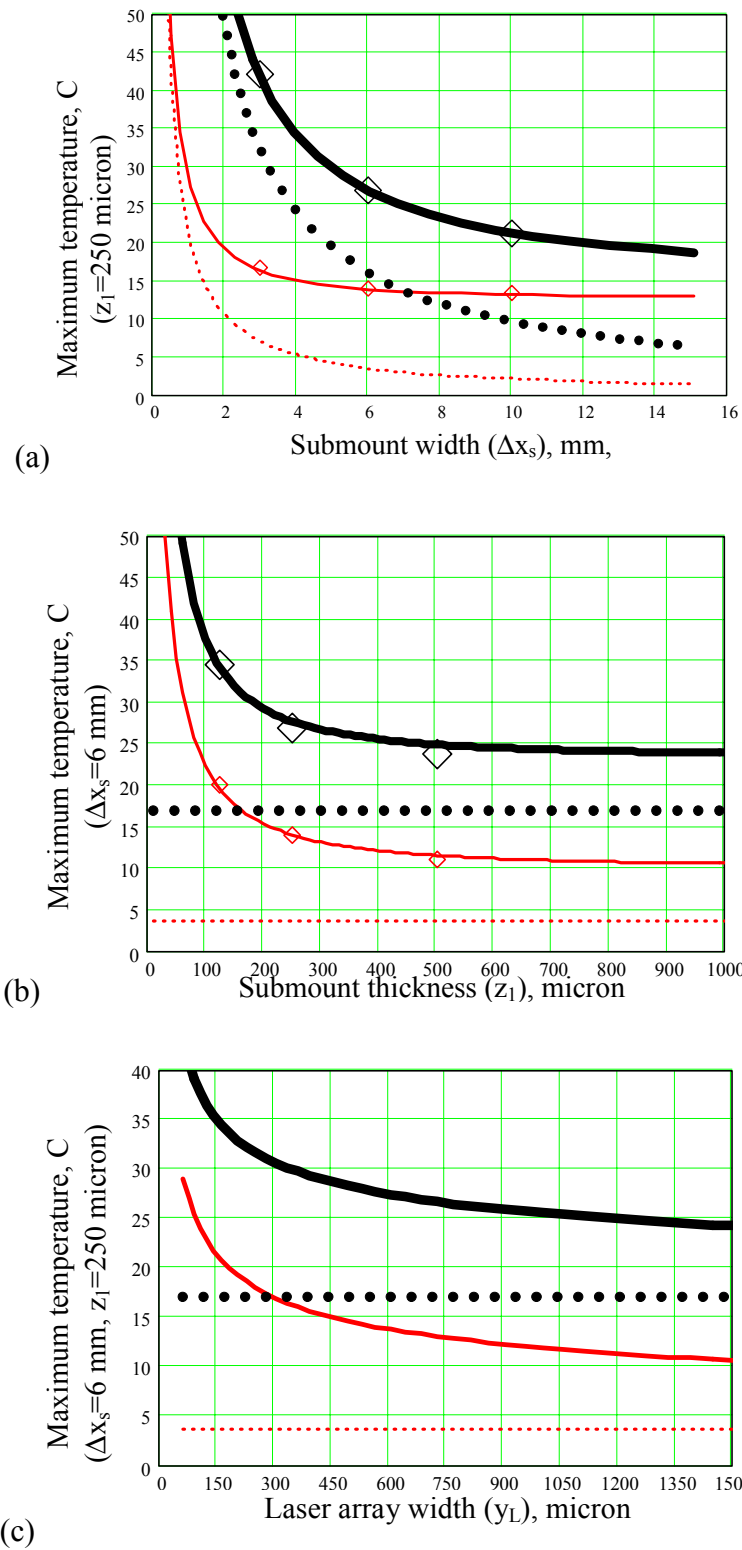


Fig. 9. Maximum temperature rise at the copper submount/laser interface relative to isothermal surface with respect to submount width (a) submount thickness (b) and laser array width (c). The heated surface is 500 by 600 μm . The submount length $\Delta y_s = 5\text{mm}$. Thin curves for submounts mounted with 100 μm silicone grease, $k_2 = 2.3\text{ W/mK}$, thick curves for submounts mounted with 200 μm thermally conductive epoxy, $k_2 = 1\text{ W/mK}$. Solid lines represent analytical solution, diamonds represent results obtained by the finite element analysis and dotted lines represent results for an ideal submount with $k_1 = \infty$.

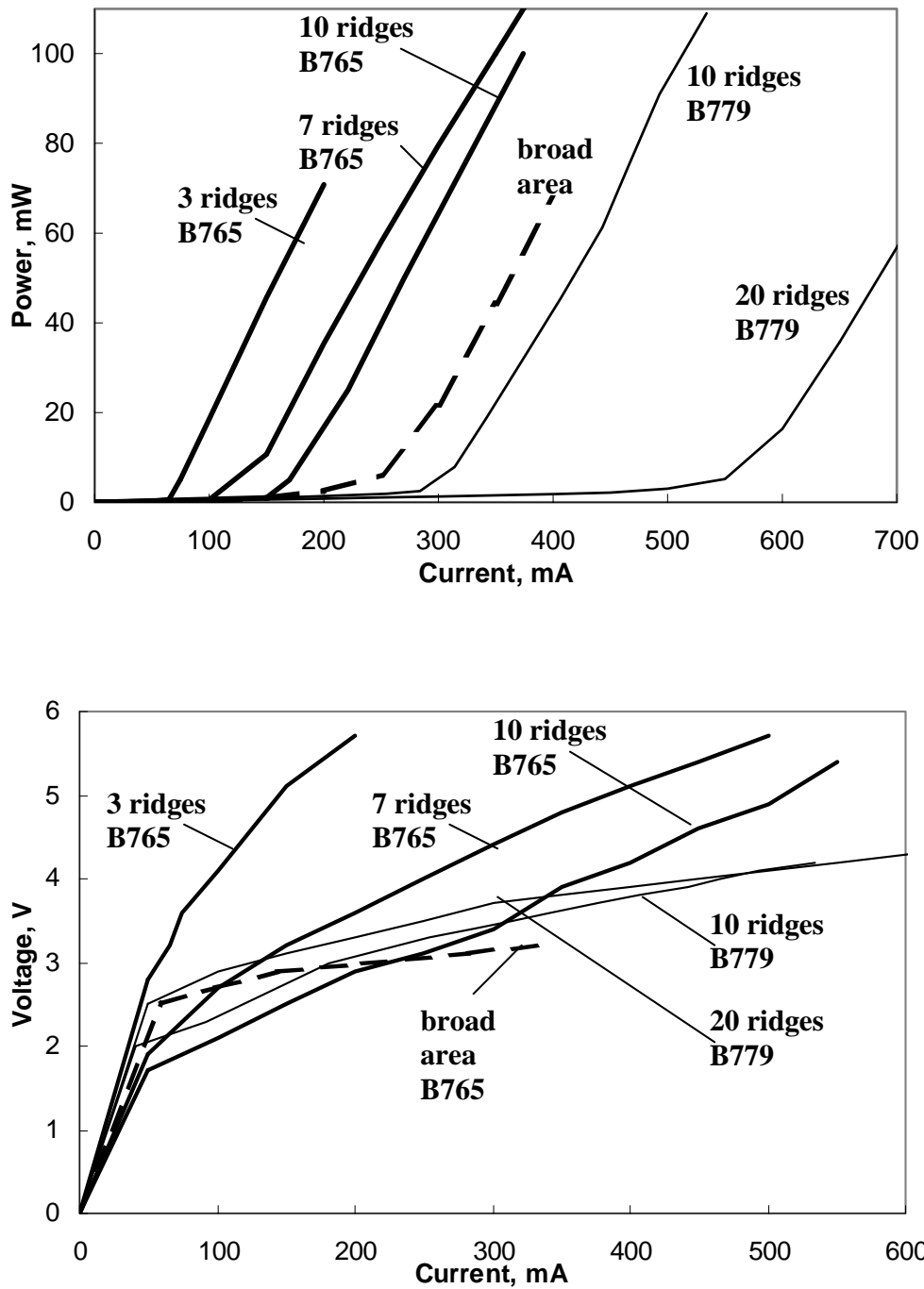


Fig. 10. Pulsed L-I and V-I curves (1 microsecond pulses and 0.1% duty cycle at a temperature of 15 C).



Fig. 11. Lasing 10 element RWG array.

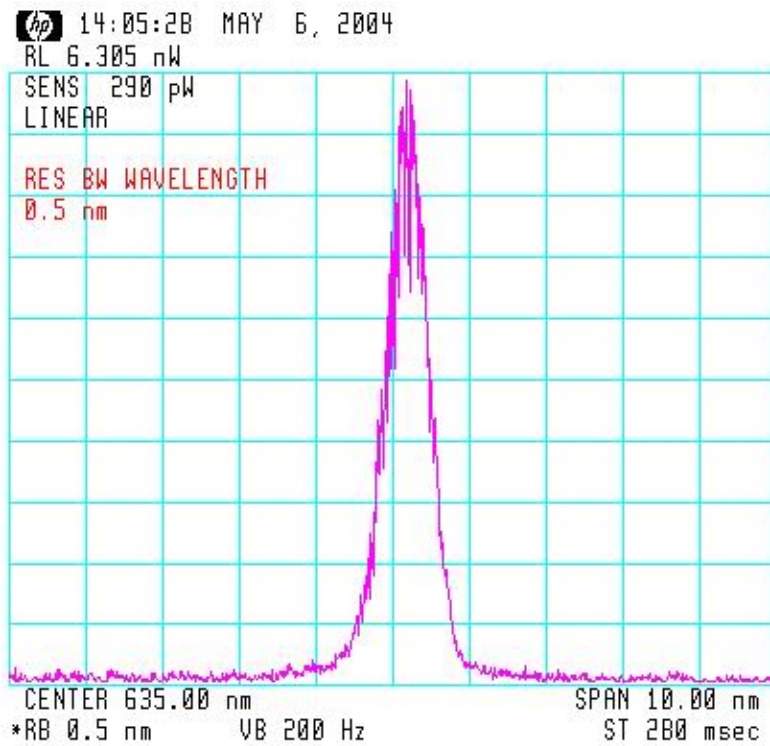


Fig. 12. Typical spectrum of a RWG array of 10 ridges

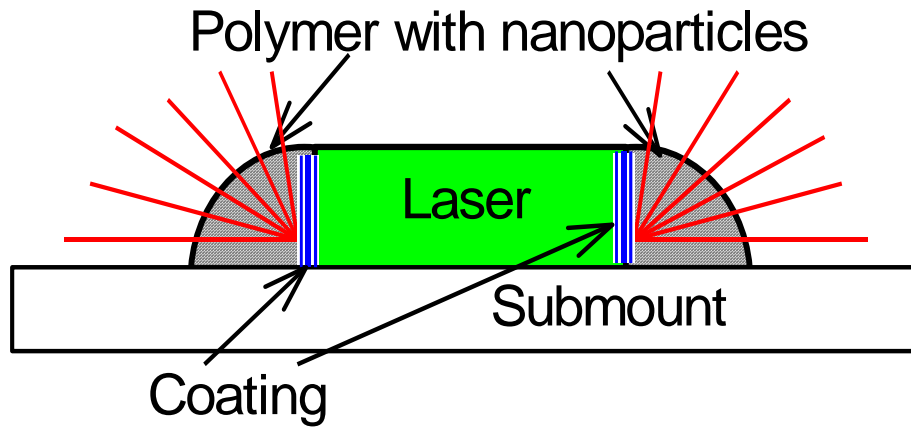


Fig. 13. Edge-emitting 635nm laser on a Cu submount with a scattering element

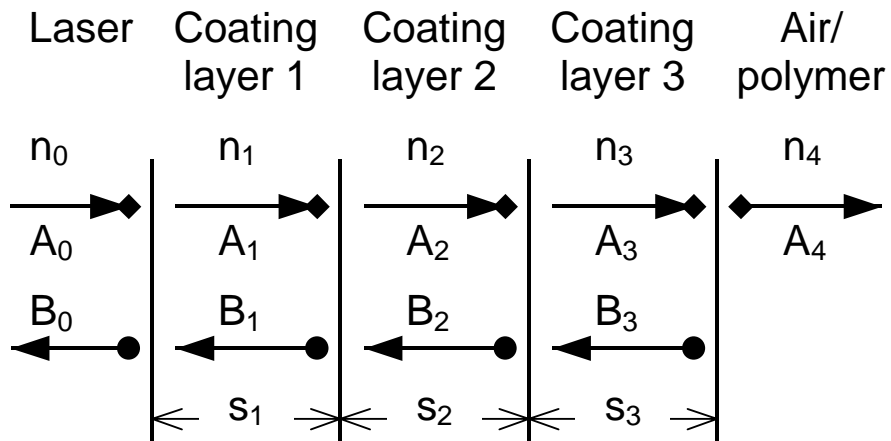


Fig. 14. 3-layer coating schematic

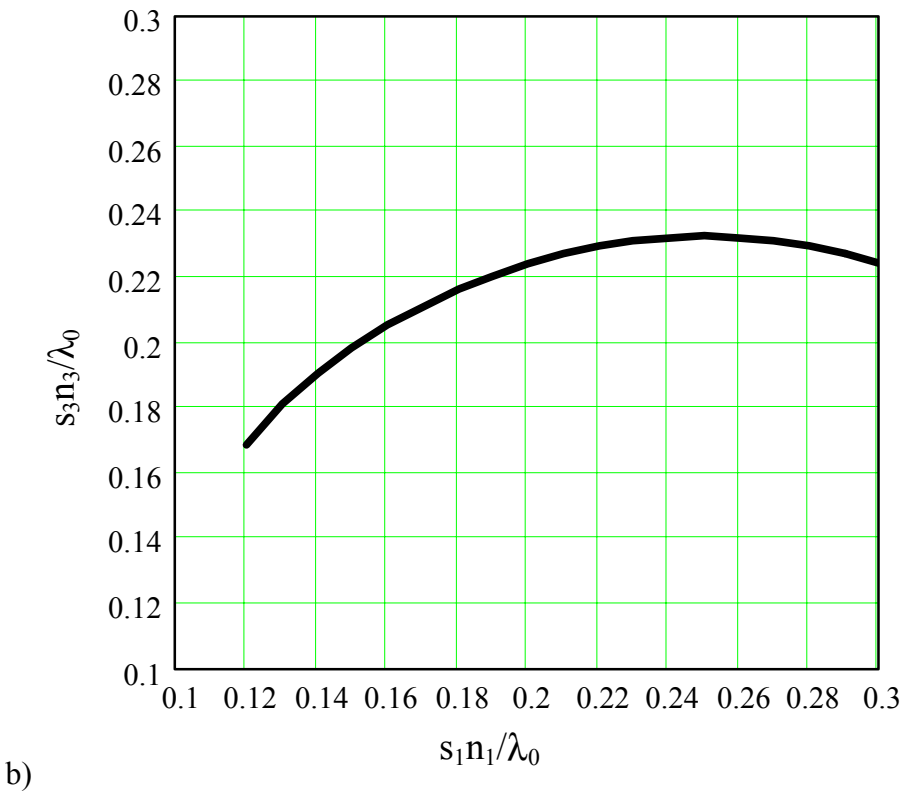
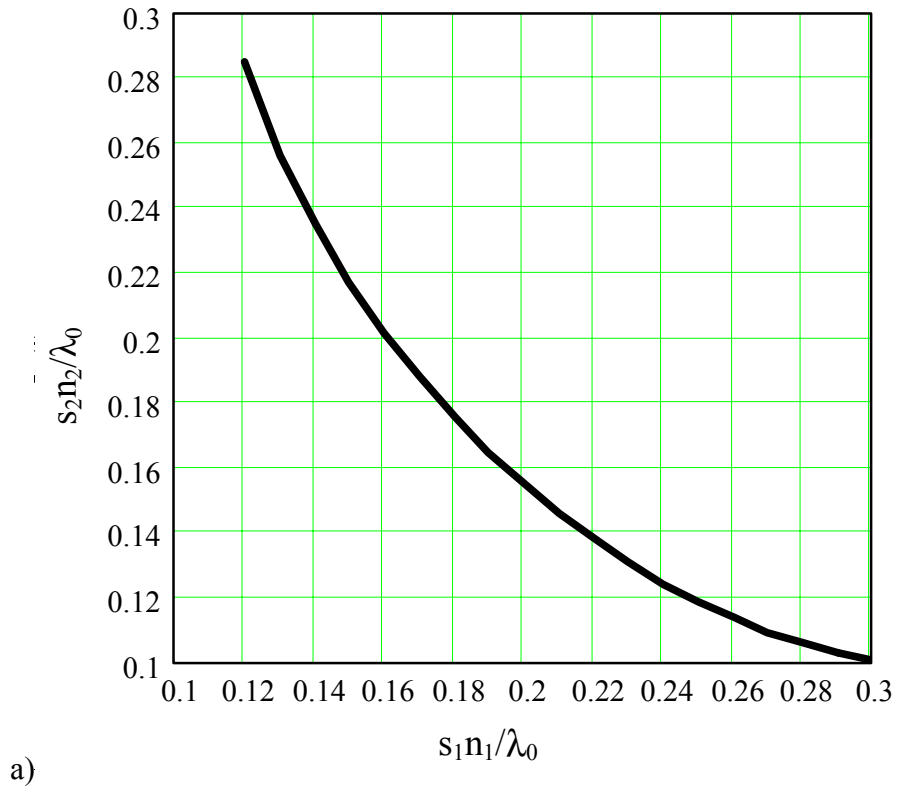


Fig. 15. Solutions for layers thickness

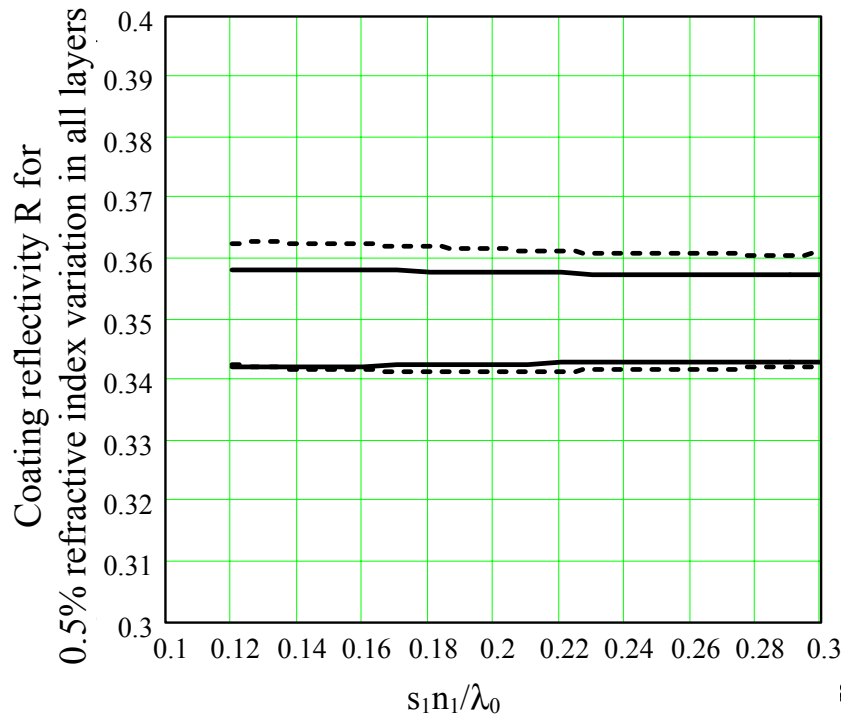
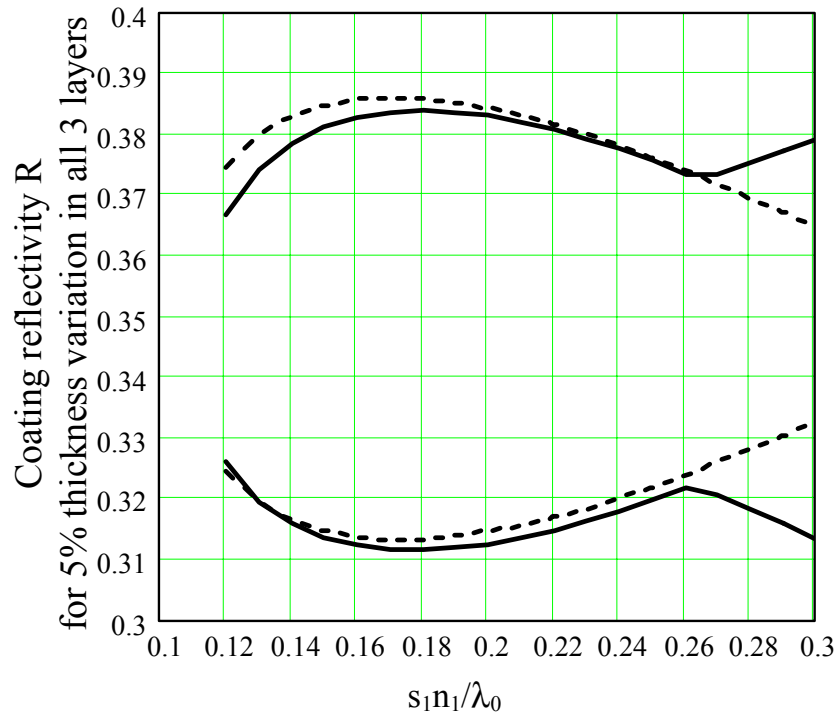


Fig. 16. Coating reflectivity R variation for 5% thickness variation in all 3 coating layers and for 0.5% refractive index variation in all layers including laser. Top and bottom curves represent min and max values of reflectivity. Solid line represents reflectivity in air, dashed line for polymer.